Surface reaction for efficient and stable inverted perovskite solar cells

Qi Jiang,[1†] Jinhui Tong,[1†] Yeming Xian,[2] Ross A. Kerner,[1] Sean P. Dunfield,[3,4] Chuanxiao Xiao,[4] Rebecca A. Scheidt,[1] Darius Kuciauskas,[1] Xiaoming Wang,[2] Matthew P. Hautzinger,[1] Robert Tirawat,[1] Matthew C. Beard,[1] David P. Fenning,[3] Joseph J. Berry,[4,5,6] Bryon W. Larson,[1] Yanfa Yan,[2*] Kai Zhu[1*]

[1] Chemistry and Nanoscience Center, National Renewable Energy Laboratory, Golden, CO 80401, USA

[2] Department of Physics and Astronomy and Wright Center for Photovoltaics Innovation and Commercialization, University of Toledo, Toledo, OH 43606, USA

[3] Department of NanoEngineering, University of California San Diego, La Jolla, CA 92093, USA

[4] Materials Science Center, National Renewable Energy Laboratory, Golden, CO 80401, USA

[5] Renewable and Sustainable Energy Institute, University of Colorado Boulder, Boulder, CO 80309, USA

[6] Department of Physics, University of Colorado Boulder, Boulder, CO 80309, USA

* Corresponding authors: Yanfa.Yan@utoledo.edu (Y.Y.); Kai.Zhu@nrel.gov (K.Z.)

[†] These authors contributed equally to this work.

Perovskite solar cells (PSCs) with an inverted structure (often referred to as the p-i-n architecture) are attractive for future commercialization due to their easily scalable fabrication, reliable operation, and compatibility with a wide range of perovskite-based tandem device architectures[1,2]. However, the power conversion efficiency (PCE) of p-i-n PSCs falls behind n-i-p (or normal) structure counterparts[3-6]. This large performance gap could undermine efforts to adopt p-i-n architectures, despite their other advantages. Given the remarkable advances in perovskite bulk materials optimization over the past decade, interface engineering has become the most important strategy to push PSC performance to its limit[7,8]. Here, we report a reactive surface engineering approach based on a simple post-growth treatment of 3-(Aminomethyl)pyridine (3-APy) on top of a perovskite thin film. First, the 3-APy molecule selectively reacts with surface FA^+, reducing perovskite surface roughness and surface potential fluctuations associated with surface steps/terraces. Second, the reaction product on the perovskite surface decreases the formation energy of charged iodine-vacancies, leading to effective n-type doping with a reduced work function in the surface region. With this reactive surface engineering, the resulting p-i-n PSCs obtained a PCE over 25%, along with retaining 87% of the initial PCE after over 2400 h of one-sun operation at about 55°C in air.

During the past decade, perovskite solar cells (PSCs) have been widely studied as a promising alternative photovoltaic (PV) technology[6]. Although the perovskite composition is still undergoing fine-tuning and improvement for specific applications, the perovskite field has accumulated various processing strategies for optimizing perovskite bulk materials, including their structure, crystallinity, defects, and other optoelectronic properties[9-11]. As a result, interface/surface modification has become vitally important to ensure further advances in the areas of charge extraction, interface recombination, and device stability[7,8,12,13]. Currently, the record single-junction PSC efficiencies are all based on n-i-p architectures, which are associated with the optimized electron transport layer (ETL) and perovskite absorber layer[8,14]. However, the standard doped hole transport layer (HTL) in the n-i-p structure presents a challenge for simultaneously achieving both high efficiency and excellent operational reliability.

The p-i-n cell structure represents an attractive option for PSC commercialization owing to its low-temperature processing and compatibility with large-scale fabrication[15,16]. Much

progress on long-term operation has been reported for p-i-n PSCs[1]. Moreover, the p-i-n structure-based perovskite tandem solar cells have demonstrated efficiencies surpassing those of single-junction PSCs[2,17,18]. Despite these attractive features, the performance of single-junction p-i-n PSCs has historically fallen behind that of n-i-p PSCs[19]. The performance of p-i-n devices has seen clear improvement in recent years, mainly due to strategies to improve perovskite quality and interfacial properties[3-5,13]. However, the performance gap is still large, and significant efforts are required to accelerate p-i-n PSC development to its full potential for various applications.

PSCs have two critical junctions at the perovskite/ETL and perovskite/HTL interfaces, and their quality has been correlated with device performance, including PCE, J-V hysteresis, and stability/reliability[20-22]. Thus, realizing high-quality junctions is key to achieving high PSC performance. During perovskite film processing, the top surface region is prone to defect formation due to easier escape of volatile species such as organic molecules and iodine (I); thus, top surface engineering is particularly important to push p-i-n PSCs to a new level. An ideal surface engineering approach for p-i-n PSCs should: (1) not negatively affect the bulk quality of the perovskite film; (2) not produce materials hindering charge transfer; (3) reduce the density of unwanted defects; and/or (4) have a surface region that creates a built-in electric field, ensuring effective electron extraction and reducing carrier recombination. Here, we demonstrate that a simple reactive surface engineering approach using the organic amine small molecule 3-(Aminomethyl)pyridine (3-APy, where Py denotes pyridine) can achieve these outcomes and, consequently, improve all PV parameters for p-i-n cells, amounting to PCE greater than 25% as well as good operational stability, i.e., retaining 87% of initial PCE for over 2400 h at ~55°C.

Surface reaction

We first explain our design strategy of selecting 3-APy for surface treatment. Creating a built-in electric field in the surface region represents a promising approach for minimizing surface recombination and enhancing charge extraction. Since good perovskite absorbers typically exhibit weak p-type conductivity or intrinsic nature, generating I-vacancies, which are shallow donors, in the surface region is a preferred method to create the built-in electric field. The formation of a positively charged I-vacancy can be promoted by introducing a molecule with a negatively charged Py-ring due to their electrostatic attraction. To allow for the incorporation of the molecule without significantly perturbing the lattice in the surface region, the molecule is better to contain a FA unit

as its head. This will allow the FA unit to be incorporated into the A site of the lattice, displaying no barrier for charge transfer. And the Py-ring unit will be left outside to promote the formation of I-vacancy nearby. 3-APy is a good candidate for this purpose. It has been shown that organic amine small molecules can react with FA 1+ cations to form bulkier amidinium 1+ cations. For example, methylamine readily reacts with FA 1+ cation, forming N-methylformamidinium 1+ cation and releasing an ammonia (NH_3) molecule[23]. 3-APy contains both a Py-ring and an amine group; expected to react with FA 1+ to form a new 1+ cation composed of a "FA cation unit" with an attached Py-ring. The reaction is depicted in **Fig. 1a**, where the surface FA^+ reacts with 3-APy, forming $MPyFA^+$ (N-(3-methylpyridine)formamidinium) and releasing NH_3. Indeed, density functional theory (DFT) calculations revealed a reaction energy of 0.72 eV, supporting a spontaneous (thermodynamically favorable) reaction. We also experimentally verified this reaction, as discussed in **Supplementary Note 1**.

We now describe the effect of 3-APy treatment of perovskite surface, whose composition is $Rb_{0.05}Cs_{0.05}MA_{0.05}FA_{0.85}Pb[I_{0.95}Br_{0.05}]_3$. The 3-APy solution was applied to the perovskite surface by spin coating. We conducted atomic force microscopy (AFM) and Kelvin probe force microscopy (KPFM) to examine the impact of 3-APy treatment on the surface topography and potential distribution. **Figure 1b** shows that for the control sample, the perovskite surface consists of clear steps (or terraced edges), which are normally an indication of highly crystalline perovskite[7,12,24]. However, the corresponding surface potential map shows that the steps cause strong potential fluctuations (**Fig. 1c**). It is worth noting that various surface defects can modify the potential distribution of the perovskite surface[25]. **Figure 1d** compares the line scan of the topography and surface potential variations from a typical perovskite region, as shown in **Figs. 1b–c**. These potential fluctuations can be up to about 50–100 mV over a length scale of about 10–20 nm. The steps on the perovskite surface are also likely more active/reactive and effective surface defects able to cause variations in local surface charge. In contrast, the 3-APy treatment drastically smoothed out these steps and suppressed the surface potential variations (**Figs. 1e–g**; more comparison in **Supplementary Fig. 7**).

The reaction-induced "polishing" effect is also verified by scanning electron microscopy (SEM) images (**Supplementary Fig. 8**)—the perovskite surface without 3-APy treatment shows obviously terraced structures, whereas the 3-APy treatment shows a much smoother surface—which is consistent with the topography results observed in **Figs. 1a,d**. This reactive

surface engineering approach showed negligible impact on X-ray diffraction (XRD) (**Supplementary Fig. 9**) and ultraviolet-visible (UV-vis) absorption (**Supplementary Fig. 10**), consistent with the 3-APy treatment being primarily a surface modification. A smoother, less defective surface is expected to be beneficial for improving the perovskite/ETL main junction[26,27].

Interfacial properties

More importantly, we found that the 3-APy treatment can modify the energetics of the perovskite surface, creating a built-in electric field that should favor electron extraction and reduce charge recombination. We utilized ultraviolet photoelectron spectroscopy (UPS) to characterize the energetics of the perovskite film with and without 3-APy treatment. The secondary electron cutoff (SECO) and the valence band maximum (VBM) spectra are displayed in **Fig. 2a**. The 3-APy treatment reduced the work function from about 4.77 eV to 4.21 eV and shifted the VBM from about 0.80 eV to 1.51 eV, creating favorable surface energetics/band bending for extracting electrons and blocking holes (**Supplementary Fig. 11**). X-ray photoelectron spectroscopy (XPS) measurements were conducted to understand chemical changes at the surface. Survey spectra, core-level spectra, and compositional ratios are displayed in **Supplementary Figs. 12–14**. The 3-APy surface treatment decreased the surface halide concentration from 42.3% (3.4 I:Pb) to 36.4% (2.5 I:Pb), increased carbon from 19.1% to 25.5%, and slightly reduced nitrogen from 22.8% to 20.6%, consistent with some of the proposed reaction product anchoring to the surface and some washing away. The 3-APy treatment also caused changes in the C 1s and N 1s core levels, which are displayed qualitatively in **Figs. 2b–c**; fits are displayed in **Supplementary Figs. 15a–d.** The control sample has a C 1s bonding environment dominated by the N^{+}=$\underline{C}H$-N amidine bonds from FA (~288 eV), with smaller contributions from $\underline{C}H_3$-N (~286 eV) bonds from MA, adventitious carbon ($\underline{C}$-C/$\underline{C}$=C) bonds (~285 eV), and carboxyl ($\underline{C}$-O/$\underline{C}$=O) bonds (~286 to 289 eV). Both the MA and FA bonds are also visible in the N 1s spectrum at ~402 eV and ~400.5 eV, respectively[28]. Upon 3-APy treatment, we see a general increase in signal across the C 1s environment, particularly at lower binding energy (BE), where bonds with fewer N groups and lower coordination are expected. This increase is dominated by enhancements to signal at ~285 eV and ~287 eV that are consistent with the $\underline{C}$-C/$\underline{C}$=C and N-$\underline{C}H_2$-C bonds of 3-APy, respectively, and the emergence of a new peak between them that is consistent with the C=$\underline{C}H$-N/C-$\underline{C}H$=N pyridinic bonds of 3-APy (**Supplementary Figs. 15e–f**)[29]. Turning to the N 1s, we see a slight increase in

the higher BE peak that is consistent with the proposed reaction, which converts one of the lower BE C=$\underline{N}H_2^+$/C-$\underline{N}H_2$ amidine bonds from FA to a pyrrolic *C*-$\underline{N}$*H*-*C* bond[28]. Moreover, we see no significant change to the peak at a lower BE, consistent with the aforementioned reaction being compensated by signals from the pyridinic C-$\underline{N}$=C group of 3-APy[30,31].

The iodine deficiency is consistent with the observed effective n-type doping and reduced work function associated with 3-APy treatment, because an I-vacancy (V_I) is a shallow donor[32]. We also conducted DFT calculations to understand the mechanism leading to the observed n-type Fermi-level shift induced by the 3-APy surface treatment. For simplification, we chose $FAPbI_3$ for DFT modeling, as it represents the main component used in this study. The DFT results are shown in **Figs. 2d–g**. We found that transforming surface FA^+ via 3-APy treatment into $MPyFA^+$ (a reaction product) on the surface can reduce the formation energy of a charged V_I by 0.19 eV. This reduced formation energy is consistent with the observed I-deficiency and effective n-type doping in the surface region upon 3-APy treatment, and it is mainly due to the electrostatic attraction between the positive charge of the V_I and the negative charge on the Py-ring side of $MPyFA^+$, which is consistent with the significant rearrangement of the MPyFA cation (**Figs. 2f, g**).

Optoelectronic properties

We conducted transient reflection (TR) spectroscopy to study the effect of 3-APy treatment on surface charge carrier dynamics (**Figs. 3a–b**; **Supplementary Note 2**). With the 3-APy treatment, the effective surface recombination velocity (*SRV*) decreased one order of magnitude, from about 1.9×10^3 cm/s (control) to 0.2×10^3 cm/s (target). The 10× reduction of *SRV* with 3-APy treatment is consistent with the improved surface potential distribution and the surface field induced by the n-type Fermi-level shift associated with the treatment. Furthermore, time-resolved microwave conductivity (TRMC) measurements showed an improved average weighted carrier lifetime (from about 1.7 μs to 2.1 μs; **Supplementary Table 1**) with the 3-APy treatment (**Fig. 3c**).

Another good way to investigate optoelectronic properties is to measure the absolute photoluminescence (PL) of the devices. The PL intensity is a direct measure of the carrier density in the perovskite absorber and the corresponding quasi-Fermi level splitting (QFLS). **Figure 3d** compares the absolute intensity PL of the control and target perovskite films in the p-i-n device configuration. The external radiative efficiency (ERE) increased from about 0.4±0.1% (control) to

2.0±0.1% (target) at about one-sun equivalent photon fluence (~1.7×10^{17} $cm^{-2}s^{-1}$) (**Supplementary Note 3**). This corresponds to a 42-mV gain in QFSL, which is associated with the reduction of nonradiative recombination enabled by the 3-APy treatment. The inset in **Fig. 3d** shows that after the 3-APy treatment, the slope of integrated PL intensity vs. excitation fluence decreased from about 1.9±0.1 to 1.6±0.1, indicating reduced interface recombination[33].

Device characteristics

We examined the impact of 3-APy treatment on the device characteristics using a typical p-i-n cell stack: glass/ITO/MeO-2PACZ/$Rb_{0.05}Cs_{0.05}MA_{0.05}FA_{0.85}Pb(I_{0.95}Br_{0.05})_3$/LiF/$C_{60}$/ bathocuproine (BCP)/Ag, where MeO-2PACZ is a self-assembled monolayer (SAM) for hole-selective contact[34]. A typical cross-sectional SEM of the device stack is shown in **Supplementary Fig. 16**. The perovskite film thickness is ~860 nm, with grains spanning across the film thickness. **Figure 4a** compares the PSCs based on the pristine perovskite (control) and 3-APy-treated perovskite (target). The 3-APy treatment increased PCE from 23.39% (reverse)/22.18% (forward) to 25.49% (reverse)/25.27% (forward), due to improvements in all parameters (**Supplementary Table 2**). The corresponding stabilized power output (SPO) were 22.85% and 25.35% for the control and target devices, respectively (**inset of Fig. 4a**). Moreover, J_{sc} reached >26 mA/cm^2 for the target cell, which is consistent with the external quantum efficiency (EQE) results (**Fig. 4b**). Analysis of the EQE spectrum suggests a bandgap of ~1.53 eV (**Supplementary Fig. 17**), which is consistent with the optical absorption measurement (**Supplementary Fig. 9**). Note that the device hysteresis is also reduced for the target device. The improvements in these PV parameters validate the hypothesis that the observed enhancement in structural/interfacial/optoelectronic properties associated with 3-APy treatment, as discussed in connection with **Figs. 1–3**, is directly relevant to PV performance. The combination of the improved J_{sc}, open-circuit voltage (V_{oc}), and fill factor (FF) was further verified based on statistical comparison of the PV parameters from 72 control and 246 target devices, with an average PCE enhancement from 22% to 24.4% (**Supplementary Fig. 18**). Among these target devices, a maximum V_{oc} of ~1.19 V (**Supplementary Fig. 19**) and a maximum FF of ~86% (**Supplementary Fig. 20**) were achieved, both with PCEs of ~25%. These results further attest to the effectiveness of the reactive surface modification with 3-APy in improving the interface for enhancing charge extraction with reduced recombination loss. One such device was measured by an accredited PV laboratory, obtaining a

certified *stabilized* PCE of 24.05±0.48% using an 11-point Asymptotic P_{max} Scan protocol (**Supplementary Fig. 21**), along with J-V scans yielding a reverse-scan PCE of 25.37% and forward-scan PCE of 25.06% (**Supplementary Fig. 22**).

We found that our reactive surface treatment also worked effectively for other FA-based perovskites (**Supplementary Figs. 23 and 24**) as well as various 3-APy-related molecules (**Supplementary Fig. 25**), making our approach a general strategy for improving p-i-n device performance. It is worth noting that surface treatment using the 3-APy-based iodide salt (3-APyI_2)—which can form a 2D surface layer—does not improve p-i-n device performance (**Supplementary Fig. 26**), likely due to interfacial energy misalignment[13]. Furthermore, 3-APy surface treatment in n-i-p devices significantly decreased device performance (**Supplementary Figs. 27 and 28**), which confirms that n-type surface doping is ideal for p-i-n device operation, but it is detrimental to n-i-p devices. This result underscores the broader importance of designing surface treatment strategies that are both chemistry and functionality-specific to a particular charge extraction interface.

Finally, we investigated the operational reliability of encapsulated devices aged under continuous light illumination at ~55°C in ambient air (**Fig. 4c**). These devices were biased with fixed resistance loads near the maximum power point during illumination. The target device retained ~87% of its initial maximum PCE after 2428 h, whereas the control kept only 76% over 1368 h. We further examined the operation stability of unencapsulated target device at 65°C under 1.2-sun continuous illumination in N_2 (ISOS-L-2I). The device retained 90% of its maximum PCE after 1315 h (**Supplementary Fig. 29a**). Moreover, the damp heat (85°C and 85% RH; ISOS-D-3) test showed that the device retained 94% of its maximum PCE after 850 h (**Supplementary Fig. 29b**). Taken together, our results suggest that the reactive surface engineering using 3-APy is an effective approach to significantly enhance p-i-n PSC performance to new state-of-the-art levels of efficiency and operational reliability.

References

1 Bai, S. *et al.* Planar perovskite solar cells with long-term stability using ionic liquid additives. *Nature* **571**, 245-250 (2019).

2 Al-Ashouri, A. *et al.* Monolithic perovskite/silicon tandem solar cell with> 29% efficiency by enhanced hole extraction. *Science* **370**, 1300-1309 (2020).

3 Li, X. *et al.* Constructing heterojunctions by surface sulfidation for efficient inverted perovskite solar cells. *Science* **375**, 434-437 (2022).

4 Azmi, R. *et al.* Damp heat–stable perovskite solar cells with tailored-dimensionality 2D/3D heterojunctions. *Science*, eabm5784 (2022).
5 Li, Z. *et al.* Organometallic-functionalized interfaces for highly efficient inverted perovskite solar cells. *Science* **376**, 416-420 (2022).
6 National Renewable Energy Laboratory, Best research-cell efficiency chart; www.nrel.gov/pv/cell-efficiency.html.
7 Jiang, Q. *et al.* Surface passivation of perovskite film for efficient solar cells. *Nat. Photonics* **13**, 460-466 (2019).
8 Min, H. *et al.* Perovskite solar cells with atomically coherent interlayers on SnO_2 electrodes. *Nature* **598**, 444-450 (2021).
9 Luo, D., Su, R., Zhang, W., Gong, Q. & Zhu, R. Minimizing non-radiative recombination losses in perovskite solar cells. *Nat. Rev. Mater.* **5**, 44-60 (2020).
10 Dunfield, S. P. *et al.* From defects to degradation: A mechanistic understanding of degradation in perovskite solar cell devices and modules. *Adv. Energy Mater.* **10**, 1904054 (2020).
11 Jeon, N. J. *et al.* Solvent engineering for high-performance inorganic–organic hybrid perovskite solar cells. *Nat. Mater.* **13**, 897-903 (2014).
12 Kim, M. *et al.* Conformal quantum dot–SnO_2 layers as electron transporters for efficient perovskite solar cells. *Science* **375**, 302-306 (2022).
13 Chen, H. *et al.* Quantum-size-tuned heterostructures enable efficient and stable inverted perovskite solar cells. *Nat. Photonics* **16**, 352-358 (2022).
14 Zhao, Y. *et al.* Inactive $(PbI_2)_2RbCl$ stabilizes perovskite films for efficient solar cells. *Science* **377**, 531-534 (2022).
15 Park, N.-G. & Zhu, K. Scalable fabrication and coating methods for perovskite solar cells and solar modules. *Nat. Rev. Mater.* **5**, 333-350 (2020).
16 Deng, Y. *et al.* Defect compensation in formamidinium–caesium perovskites for highly efficient solar mini-modules with improved photostability. *Nat. Energy* **6**, 633-641 (2021).
17 Lin, R. *et al.* All-perovskite tandem solar cells with improved grain surface passivation. *Nature*, 1-9 (2022).
18 Tong, J. *et al.* Carrier control in Sn–Pb perovskites via 2D cation engineering for all-perovskite tandem solar cells with improved efficiency and stability. *Nat. Energy* **7**, 642-651 (2022).
19 Lin, X. *et al.* Efficiency progress of inverted perovskite solar cells. *Energy Environ. Sci* **13**, 3823-3847 (2020).
20 Chen, C. *et al.* Arylammonium-assisted reduction of the open-circuit voltage deficit in wide-bandgap perovskite solar cells: the role of suppressed ion migration. *ACS Energy Lett.* **5**, 2560-2568 (2020).
21 Xiao, C. *et al.* Junction quality of SnO_2-based perovskite solar cells investigated by nanometer-scale electrical potential profiling. *ACS Appl. Mater. Interfaces* **9**, 38373-38380 (2017).
22 Hou, Y. *et al.* Efficient tandem solar cells with solution-processed perovskite on textured crystalline silicon. *Science* **367**, 1135-1140 (2020).
23 Wang, X. *et al.* Perovskite solution aging: what happened and how to inhibit? *Chem* **6**, 1369-1378 (2020).
24 Jang, Y.-W. *et al.* Intact 2D/3D halide junction perovskite solar cells via solid-phase in-plane growth. *Nat. Energy* **6**, 63-71 (2021).

25 Stecker, C. *et al.* Surface defect dynamics in organic–inorganic hybrid perovskites: from mechanism to interfacial properties. *ACS Nano* **13**, 12127-12136 (2019).
26 McGott, D. L. *et al.* 3D/2D passivation as a secret to success for polycrystalline thin-film solar cells. *Joule* **5**, 1057-1073 (2021).
27 Kuciauskas, D. *et al.* Recombination velocity less than 100 cm/s at polycrystalline Al_2O_3/CdSeTe interfaces. *Appl. Phys. Lett* **112**, 263901 (2018).
28 Martins, N. C. *et al.* N-doped carbon quantum dots/TiO_2 composite with improved photocatalytic activity. *Appl. Catal. B: Environ.* **193**, 67-74 (2016).
29 Gabka, G. *et al.* Ligand exchange in quaternary alloyed nanocrystals–a spectroscopic study. *Phys. Chem. Chem. Phys.* **16**, 23082-23088 (2014).
30 Osadchii, D. Y., Olivos-Suarez, A. I., Bavykina, A. V. & Gascon, J. Revisiting nitrogen species in covalent triazine frameworks. *Langmuir* **33**, 14278-14285 (2017).
31 Rabchinskii, M. K. *et al.* From graphene oxide towards aminated graphene: Facile synthesis, its structure and electronic properties. *Sci. Rep.* **10**, 1-12 (2020).
32 Yin, W.-J., Shi, T. & Yan, Y. Unusual defect physics in $CH_3NH_3PbI_3$ perovskite solar cell absorber. *Appl. Phys. Lett* **104**, 063903 (2014).
33 Sarritzu, V. *et al.* Optical determination of Shockley-Read-Hall and interface recombination currents in hybrid perovskites. *Sci. Rep.* **7**, 1-10 (2017).
34 Al-Ashouri, A. *et al.* Conformal monolayer contacts with lossless interfaces for perovskite single junction and monolithic tandem solar cells. *Energy Environ. Sci* **12**, 3356-3369 (2019).

Figure Legends

Fig. 1. Surface reaction, topography, and potential. a, Condensation reaction scheme of FA^+ and 3-APy. **b–d,** Atomic force microscopy (AFM) topography image (**b**), Kelvin probe force microscopy (KPFM) surface potential image (**c**), and the corresponding line profiles (**d**) for the perovskite film without surface treatment. **e–g,** AFM, KPFM, and line profile comparison, respectively, for the perovskite film with 3-APy surface treatment. Note that the KPFM images were flattened by subtracting a constant baseline potential (-2.4 V for the untreated and -1.7 V for the treated sample) for a better comparison of the potential variations.

Fig. 2. Surface chemistry and energetics. a, Ultraviolet photoelectron spectroscopy (UPS) measurements for perovskite films without (control, black) and with (target, red) 3-APy treatment. The work function (W_F) and valence band maximum (VBM) results are indicted. **b, c,** Comparison of the X-ray photoelectron spectroscopy (XPS) spectra of N 1s (**b**) and C 1s (**c**) core levels for the control (black) and the 3-APy treated (red) perovskite films. The expected peak locations of relevant bonding environments are labeled. **d–g,** Density functional theory (DFT) modeling of the impact of 3-APy and perovskite interaction on the charged I-vacancy formation. Side view (left) and top view (right) of the atomic structures of the pristine perovskite without (**d**) and with (**f**) 3-

APy modification, and the corresponding atomic structures with one I-atom removed (**e** and **g**). The removed I-atom is indicated by the orange color in (**d** and **f**).

Fig. 3. Optoelectronic properties. a, b, Comparison of transient reflection (TR) spectroscopy measurements of the control perovskite film (**a**) and the target perovskite film with 3-APy surface reaction (**b**) to study the carrier diffusion and surface recombination dynamics. **c,** Comparison of normalized time-resolved microwave conductivity (TRMC) transients of the control and target perovskite films. Dashed lines are the best fits to a biexponential function that includes the 5-ns pulse width generation term. **d,** Comparison of absolute intensity photoluminescence (PL) spectra at about one sun (~1.7×10^{17} photons $cm^{-2}s^{-1}$), along with the intensity dependence (inset), of representative p-i-n devices based on the control and target perovskite films.

Fig. 4. Device characteristics. a, Photocurrent density-voltage (J-V) curves of the champion control and target (with 3-APy surface treatment) p-i-n PSCs under one-sun (100 mW/cm^2) illumination. The inset shows the corresponding stabilized power output (SPO) efficiencies. **b,** Comparison of the external quantum efficiency (EQE) spectra with the integrated short-circuit current density (J_{sc}) of 25.17 mA/cm^2 and 25.74 mA/cm^2 for the control and target, respectively. **c,** Stability of encapsulated control and target devices, held under resistive load (560 ohm) near the maximum power point, under 1-sun illumination at 55±2°C in air with 40-60% RH (relative humidity). The initial device PCE was 22.3% for the control and 24.6% for the target. The devices were encapsulated with cover glass and epoxy (Gorilla 2 Part 4200101-2 Epoxy).

METHODs

Materials

RbI (99.99%), CsI (99.99%), PbI_2 (99.999%), and 3-APy were purchased from Sigma-Aldrich. Organic salts of FAI and MABr were purchased from Greatcell Solar Materials (Australia); $PbBr_2$ and MeO-2PACZ were purchased from Tokyo Chemical Industry (TCI). Dimethylformamide (DMF, 99.8%, anhydrous), dimethyl sulfoxide (DMSO, 99.9%, anhydrous), chlorobenzene (99.9%, anhydrous), and toluene (99.9%, anhydrous) were purchased from Sigma-Aldrich. For evaporating materials, LiF was purchased from Alfa Aesar, C60 was purchased from Lumtec, and BCP was purchased from Sigma-Aldrich. All chemicals were used directly as received.

Perovskite precursor solution

The perovskite composition is $Rb_{0.05}Cs_{0.05}MA_{0.05}FA_{0.85}Pb(I_{0.95}Br_{0.05})_3$. The perovskite precursor was prepared in mixed solvents of DMF:DMSO (volume ratio 4:1). The chemical molar ratio of CsI, RbI, FAI, PbI_2, $PbBr_2$, MABr is 0.05, 0.05, 0.85, 0.95, 0.05, 0.05, and the concentration is 1.5 M.

Synthesis of 3-picolyamine iodide salt (3-APyI_2)

A mixture of 3-picolyamine (1.50 mL, 14.7 mmol) and ethanol (50 mL) was added to a round-bottom flask and cooled in an ice bath. While rapidly stirring, a slight excess of concentrated hydroiodic acid (4.75 mL, 31.0 mmol) was slowly added. After stirring for 1 h, a precipitate had formed and was removed from the mixture via vacuum filtration and washed with diethyl ether (4 × 50 mL). The product was then dried overnight at 55°C under vacuum.

Device fabrication

The patterned transparent conducting oxide glass substrates (ITO or FTO) were washed with acetone and isopropanol for 15 min each. After UV Ozone treatment for 15 min, a 0.5 mg/mL MeO-2PACZ SAM solution dissolved in ethanol was spin-coated on substrates at 3000 r.p.m. for 30 s in a nitrogen glovebox, followed by annealing at 100°C for 10 min. The perovskite composition is $Rb_{0.05}Cs_{0.05}MA_{0.05}FA_{0.85}Pb(I_{0.95}Br_{0.05})_3$, and the initial stock perovskite solution is 1.5 M. In detail, CsI (19.5 mg), RbI (15.9 mg), MABr (8.4 mg), FAI (219.5 mg), PbI_2 (656.9 mg) and $PbBr_2$ (27.5 mg) were dissolved in 1 mL mixed solvent of DMF:DMSO (v:v=4:1), shaken by a Vortex Shaker for about 1-2 h to make it fully dissolved. The 1.5-M perovskite precursor solution, without filtering and dilution, was used for preparing perovskite films. Perovskite precursor solutions prepared on the same day or aged within about two weeks (in sealed vials) can be used, without noticeable impact on device performance. We used SCS G3 Spin Coater (Model: G3P8) for spin-coating. No intentional acceleration steps were used during spin-coating; the target spin speed can be reached within 1 s. Specifically, the substrate was first spinning at 1000 rpm (within 1 s from 0 to 1000; no slow acceleration steps) for 10 s, and then at 3000 rpm (no slow acceleration steps) for 40 s. After 15 s into the second stage (3000 rpm, 40 s), 150 µL chlorobenzene antisolvent was dropped on top of the spinning substrates (~1 cm distance). The perovskite sample was subsequently annealed at 100°C for 10 min. For 3-APy treatment, the diluted toluene solution of 3-APy (0.1 mM) was spin-coated on the perovskite surface at 5000

r.p.m. for 30 s, followed by annealing at 70°C for 5 min. Afterward, samples were transferred to an Angstrom evaporator for LiF (1 nm)/C60 (30 nm)/BCP (6 nm)/Ag (100 nm) deposition. The device area by evaporation was 0.112 cm^2. Unless otherwise stated, the devices were masked with metal aperture masks (0.059 cm^2) during the J-V measurement.

KPFM characterizations

KPFM measurements were performed on a D5000 atomic force microscope inside an Ar-filled glovebox. We used a Pt-Ir-coated silicon probe (PPP-EFM) in tapping mode. The plane-view samples were scanned in at least three random locations to ensure reliable measurements. The mapping contains 1024 pixels in the fast-scan axis and 256 lines in the slow-scan axis. The scan rate is 0.35 Hz.

XPS and UPS measurement

XPS and UPS measurements were performed on a Kratos AXIS-Supra in the Surface Science Facility at the UC Irvine Materials Research Institute (IMRI). X-ray radiation was produced by a monochromatic Al Kα excitation centered at 1486.6 eV. UPS radiation was produced by ionizing helium I (energy 21.22 eV). XPS survey spectra were collected using a step size of 1 eV and pass energy of 160 eV; core-level spectra were collected using a step size of 0.1 eV and pass energy of 20 eV; and UPS spectra were conducted using a step size of 0.02 eV and pass energy of 10 eV. The electron binding energy scale was calibrated using the Fermi edge and core levels of gold and silver substrates cleaned with argon-ion bombardment. To ensure that important energetic information was preserved, UPS scans and I $3d_{5/2}$ low-power XPS (1.5 W versus 225 W) scans were conducted at the beginning of analysis, each on unanalyzed locations. To attempt to account for energetic shifts arising from the beam damage that is unavoidable in the high-power core-level scans, all core levels were shifted back such that their high-power I $3d_{5/2}$ peak (225 W, 0.5 min) overlapped with the low-power peak (1.5 W, 4 min). UPS spectra were numerically corrected for satellite peaks that arose from the polychromic He radiation[35]. XPS peaks were fit using a Gaussian-Lorentzian peak-fitting algorithm with a Shirley background using the XPST package on Igor WaveMetrics. Work functions were determined using the intersection between the baseline and a linear fit to the SECO. VBMs were calculated using linear extrapolation of the valence band feature to the background signal on a semi-log plot.

TR measurement

TR measurements were performed with a Coherent laser (800-nm fundamental beam, 1-kHz rep rate, 3-mJ/pulse, and 100-fs pulse width). The fundamental beam was split into a pump and probe pulse. The probe pulse was used to generate a white light supercontinuum via a sapphire crystal that was then sent through a delay line with a time scale up to 2.5 ns. The pump pulse was tuned using a Palitra Duo optical parametric amplifier (OPA) to obtain varying excitation wavelengths. The pump and probe pulses were aligned spatially onto the sample at an approximately 45° angle to the sample surface. A Helios ultrafast spectrometer was used for detection, with the spectrometer at a 90° angle to the incident pump and probe beams. The excitation density for all TR measurements was kept so that the initial number of photogenerated charge carriers directly after pump excitation did not exceed ~4×10^{17} charge carriers/cm^3. A global fit analysis was performed on the measurements in accordance with previously reported protocols[36].

TRMC measurement

Perovskite target and control films were prepared in an identical manner to those used in devices, except onto precleaned 25×11×1-mm quartz plates (Technical Glass Products, Inc.). Microwave conductivity measurements were conducted using previously described protocols[37]. In brief, a 5-ns pulse width, 10-Hz laser at 643 nm was coupled into an X band resonant cavity to photo-generate carriers in each perovskite film, the power from which was measured before and after each measurement using a photothermal detector placed at the sample position and masked by the optical widow and waveguide sections when the sample was present. Each sample was positioned inside the microwave cavity such that excitation was always incident to the quartz side, and continuous nitrogen purge was applied to the cavity during all measurements. Neutral density filters were used to attenuate the beam power over one order of magnitude to below 10^{10} cm^{-2} absorbed photon flux. For analysis, each sample's fraction of absorbed light was measured inside an integrating sphere diffuse reflectance accessory (Cary 7000i), whereas the beam attenuation profiles of the filter combinations were extracted from the measured specular transmission data for each neutral density filter at the excitation wavelength.

PL characterization

Excitation at 632.8 nm (HeNe laser) was used to measure PL emission spectra. A Princeton Instruments HRS300 spectrograph with Si CCD (Pixis F100) and InGaAs (PyLoN IR) detectors was used. The spectral response of the detectors and spectrometer system was corrected using calibration sources (IntelliCal for vis and IR ranges, Princeton Instruments) and placing calibration sources at the sample position. Excitation beam size was determined with a CCD camera. Data was measured in absolute photon numbers using Spectralon reflectance standards (LabSphere Inc.) and assuming that one-sun equivalent fluence for 1.53-eV bandgap is about 1.73×10^{17} photons/(cm^2s).

DFT calculations

The structural relaxation and static self-consistent energy calculations are performed by CP2K package at the PBE level[38,39] A 6-layer $FAPbI_3$ perovskite slab model is constructed for the cases before and after 3-APy treatment with typical (001) orientation selected on the surface, which is terminated by FAI. The double-ξ valence polarization basis set trained from optimized molecular geometries is used in the calculations with only the gamma point considered, and the energy cutoff of 550 Ry is set. The formation energy difference of a charged iodine vacancy (V_I) on the surface region with and without 3-APy treatment is calculated by the following equation:

$$\Delta E_f = (E_w(V_I,q) - E_w) - (E_{w/o}(V_I,q) - E_{w/o})$$

where $E_w(V_I,q)$ is the total energy of the supercell with the 3-APy cation and a charged V_I, E_w is the total energy of the supercell with the 3-APy cation but without a charged V_I. $E_{w/o}(V_I,q)$ is the total energy of the supercell without the 3-APy cation but with a charged V_I, $E_{w/o}$ is the total energy of the supercell without the 3-AP cation and without a charged V_I.

Mass spectrometry (MS) measurement

The sample was diluted 1:1000 v/v in acetonitrile and analyzed with a Thermo Scientific Q-Exactive mass spectrometer equipped with a heated electrospray ionization (HESI) source. The sample was directly infused via a syringe pump at 10 µL/min, with the following source conditions: Sheath gas flow – 10 arbitrary units, Aux gas flow - 0 arbitrary units, spray voltage – +2.9 kV, capillary temperature – 320 °C, S-lens RF level – 50 V, Aux gas heater – 0 °C. Spectra were collected with a resolution of 140,000 at m/z 200 and an AGC target of 1 million. Full scan spectra were collected from m/z 50-700 and MS/MS data were collected by quadrupole isolation of m/z

136 ± 2 and fragmented with Normalized Collision Energy (NCE) values of 10 and 60 to yield the full fragmentation profile. Quasi-MS data was collected by inducing fragmentation in the source region, and isolating m/z 92 ± 2, followed by fragmentation at 60 NCE. Molecular formula assignments were based on accurate mass and ^{13}C isotopic fine structure.

Other characterizations

The optical properties of the perovskite films were measured using UV-vis spectroscopy (Cary 6000i). The crystal structures of perovskite films were recorded using an X-ray diffractometer (D-Max 2200, Rigaku). The morphologies and microstructures of the perovskite films and cross-sectional structures of the solar cells were investigated using a Hitachi S-4800 scanning electron microscope. The J-V curves were measured in a nitrogen glovebox using a Newport Oriel Sol3A class solar simulator with a xenon lamp that was calibrated before use with a silicon cell under a KG2 filter. The SPOs of the devices were measured by monitoring the photocurrent density output evolution under the biased voltage set near the maximum power point. EQE measurements were performed in ambient air using a Newport Oriel IQE200 with monochromatic light focused on the device pixels and a chopper frequency of 37 Hz.

Data availability

The data that support the findings of this study are available from the corresponding authors on reasonable request.

Additional References

35 Shallcross, R. C., Zheng, Y., Saavedra, S. S. & Armstrong, N. R. Determining band-edge energies and morphology-dependent stability of formamidinium lead perovskite films using spectroelectrochemistry and photoelectron spectroscopy. *J. Am. Chem. Soc.* **139**, 4866-4878 (2017).

36 Yang, Y. *et al.* Top and bottom surfaces limit carrier lifetime in lead iodide perovskite films. *Nat. Energy* **2**, 1-7 (2017).

37 Reid, O. G. *et al.* Quantitative analysis of time-resolved microwave conductivity data. *J. Phys. D: Appl. Phys* **50**, 493002 (2017).

38 Hutter, J., Iannuzzi, M., Schiffmann, F. & VandeVondele, J. cp2k: atomistic simulations of condensed matter systems. *Wiley Interdiscip. Rev. Comput. Mol. Sci.* **4**, 15-25 (2014).

39 Perdew, J. P., Burke, K. & Ernzerhof, M. Generalized gradient approximation made simple. *Phys. Rev. Lett.* **77**, 3865 (1996).

Acknowledgements

The work was partially supported by the U.S. Department of Energy under Contract No. DE-AC36-08GO28308 with Alliance for Sustainable Energy, Limited Liability Company (LLC), the Manager and Operator of the National Renewable Energy Laboratory. The authors acknowledge the support on first-principle calculations, surface reaction analysis, synthesis of 3-APyI_2, and optoelectronic characterizations (e.g., TR and TRMC), from the Center for Hybrid Organic-Inorganic Semiconductors for Energy (CHOISE), an Energy Frontier Research Center funded by the Office of Basic Energy Sciences, Office of Science within the U.S. Department of Energy. A portion of the research was performed using computational resources sponsored by the Department of Energy's Office of Energy Efficiency and Renewable Energy and located at the National Renewable Energy Laboratory. The authors also acknowledge the support on 3-APy surface treatment and the corresponding device fabrication and characterizations from DE-FOA-0002064 and Award Number DE-EE0008790, and the support on the general device and thin-film perovskite fabrication/characterizations from the Advanced Perovskite Cells and Modules program of the National Center for Photovoltaics, funded by the U.S. Department of Energy, Office of Energy Efficiency and Renewable Energy, Solar Energy Technologies Office. This work was also supported in part by the California Energy Commission EPIC program, EPC-19-004. We acknowledge the use of facilities and instrumentation at the UC Irvine Materials Research Institute (IMRI), which is supported in part by the National Science Foundation through the UC Irvine Materials Research Science and Engineering Center (DMR-2011967). XPS/UPS was performed in part using instrumentation funded in part by the National Science Foundation Major Research Instrumentation Program under grant no. CHE-1338173. Additionally, we would like to thank Dr. Ich Tran for assistance with collecting the XPS/UPS data. We also would like to thank Dr. Steven M. Rowland and Lieve M. Laurens for conducting the mass spectrometry measurements and structure assignments at the NREL Bioenergy Science Technologies directorate. The views expressed in the article do not necessarily represent the views of the DOE or the U.S. Government.

Author contributions

Q.J., J.T., and K.Z. conceived the idea. K.Z. supervised the projects and process. Q.J. fabricated perovskite films/devices and conducted XRD/SEM/UV-vis and stability measurements. J.T. was involved in material/device design and analysis. Y.X. carried out the DFT calculation, with help

from X.W., under the supervision of Y.Y. R.A.K. and B.W.L. were involved in surface reaction study and relevant analysis. S.P.D. performed XPS/UPS measurements and analysis under the guidance of D.P.F. C.X. performed AFM and KPFM characterizations and analysis. R.A.S. conducted TR measurement and analysis under the guidance of M.C.B. D.K. performed the PL characterization and analysis. M.P.H. prepared the 3-APy halide salts. R.T. helped to work on device stability test under the supervision of J.J.B. B.W.L. conducted the TRMC measurement and analysis. Q.J. and K.Z. wrote the first draft of the manuscript. All authors discussed the results and contributed to the revisions of the manuscript.

Competing interests

An application has been made for a provisional patent (US patent application number 63/344,265) related to the subject matter of this manuscript.

Additional information

Correspondence and requests for materials should be addressed to Yanfa Yan or Kai Zhu.

Figure 1

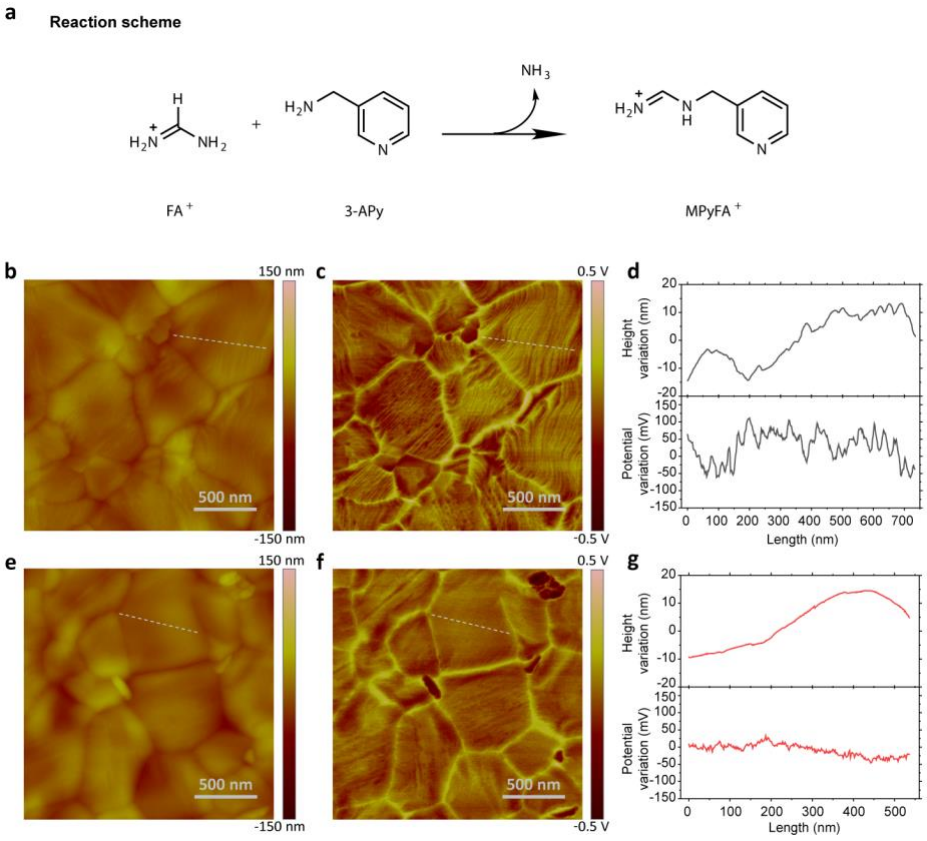

Figure 2

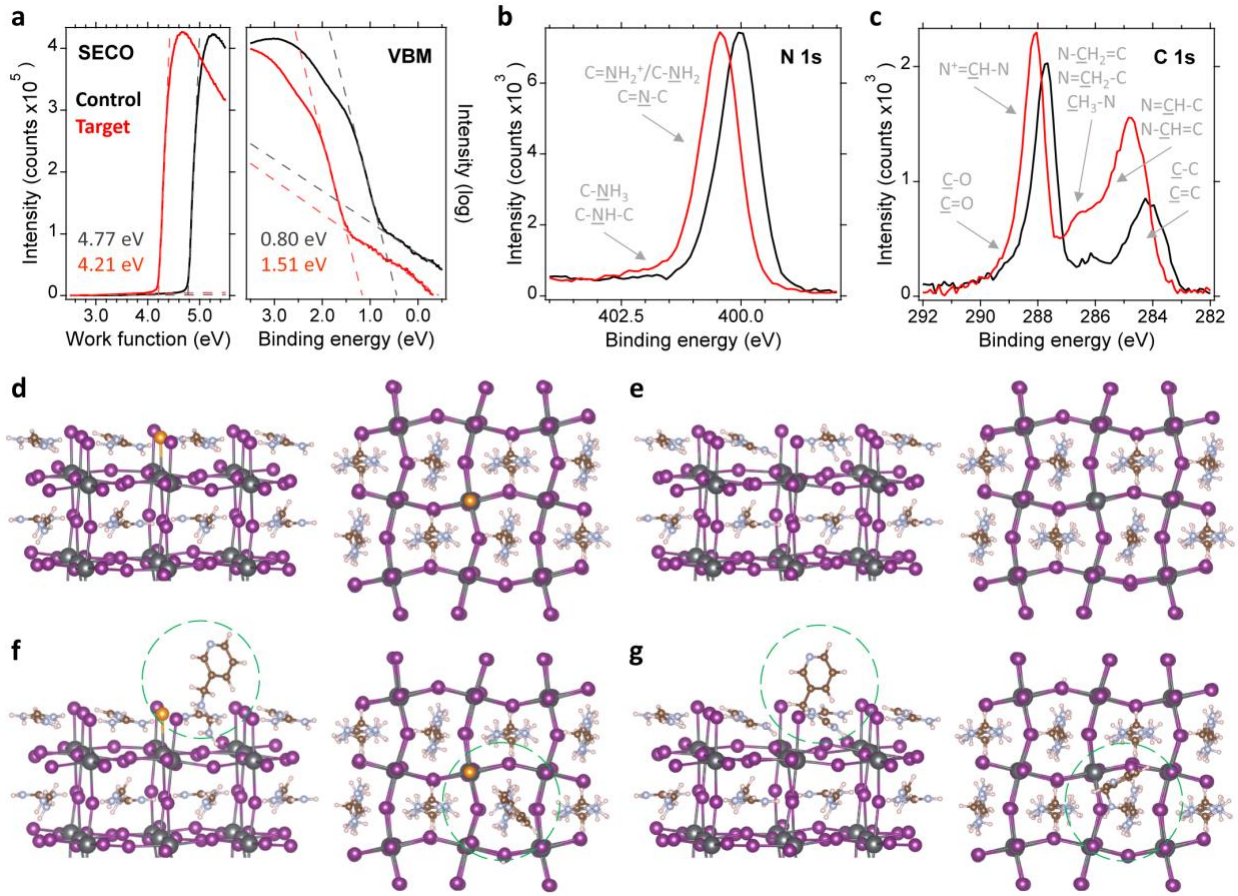

Figure 3

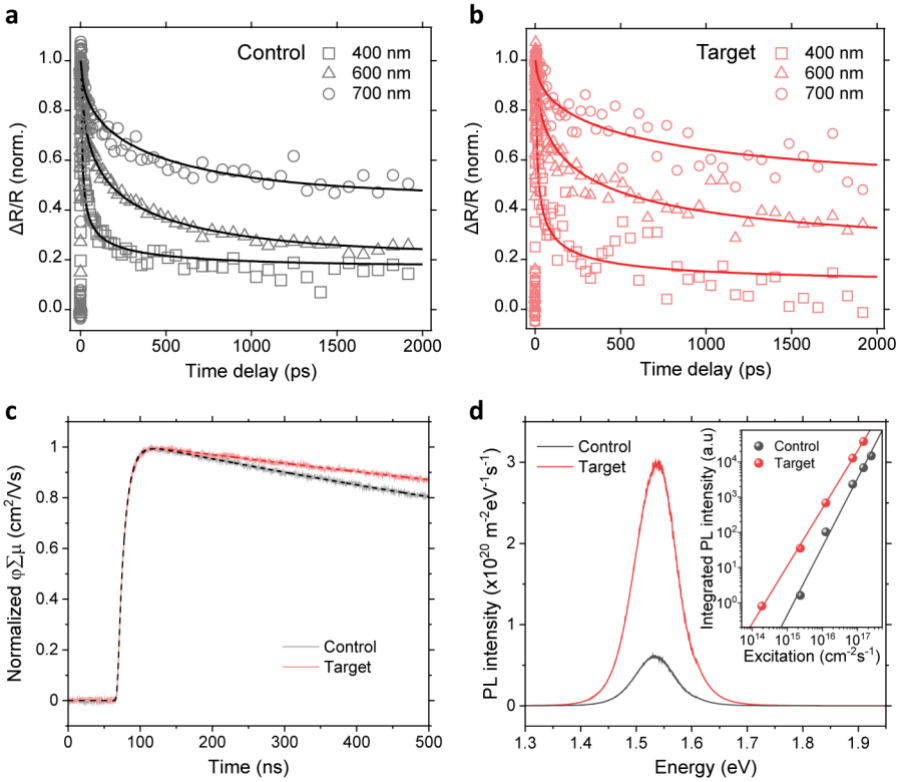

Figure 4